Research Square

Preprints are preliminary reports that have not undergone peer review.
They should not be considered conclusive, used to inform clinical practice,
or referenced by the media as validated information.

Optical Tamm states-induced tunable triple-band spin-dependent near-perfect absorption in a magnetic Weyl semimetal-Fibonacci heterostructure

Jipeng Wu

jipengwu243@163.com

Yulei Liao
Lingfeng Liao
Yating Wang
Jing Liu
Jiaxuan Liu
Rongzhou Zeng

Research Article

Keywords: Magnetic Weyl semimetals, Optical Tamm states, Spin-dependent absorption, Fibonacci quasi-periodic photonic crystal

Posted Date: September 25th, 2026

DOI: https://doi.org/10.21203/rs.3.rs-10831175/v1

License: This work is licensed under a Creative Commons Attribution 4.0 International License.
Read Full License

Additional Declarations: No competing interests reported.

Abstract

Magnetic Weyl semimetals (mWSMs) enable spin-resolved optical responses at zero magnetic field via their intrinsic topological magneto-optical effects, making them an ideal material platform for spin-selective absorption. However, most existing mWSM-based absorption structures rely on periodic photonic crystal, whose single resonance channel is insufficient to support multichannel parallel spin information processing. Here we construct a heterostructure composed of a Fibonacci quasi-periodic photonic crystal and an mWSM thin film, and systematically investigate its spin-dependent absorption characteristics by using the 4×4 transfer matrix method. Results show that the self-similar fractal energy bands of the quasi-periodic structure satisfy the optical Tamm states phase matching condition in three reflection bandgaps simultaneously, inducing triple-band near-perfect absorption with prominent spin splitting in each band. Furthermore, Weyl node separation, Fermi level and dielectric layer thickness act as independent tuning parameters to adjust the resonance frequency and absorption intensity of the three absorption bands respectively. This study breaks the channel number limitation of periodic configurations and provides a feasible approach for designing integrated multichannel spin photonic devices.

Introduction

Conventional magneto-optical materials, such as yttrium iron garnet and bismuth iron garnet, exhibit weak intrinsic magneto-optical responses and rely on external magnetic fields to break time-reversal symmetry for spin resolution. The resulting bulky devices and complex systems impose severe constraints on miniaturization and integration [1–3]. Alternative approaches, including chiral metasurfaces and magneto-optically modified two-dimensional materials, are limited by intricate fabrication processes and single-channel operation modes [4–6]. Therefore, realizing efficient multi-band spin-dependent absorption under zero magnetic field has emerged as a critical challenge awaiting breakthroughs in photonics.

Magnetic Weyl semimetals (mWSMs) offer an ideal material platform for spin-dependent absorption. The Berry curvature in momentum space functions as an intrinsic effective magnetic field, giving rise to the anomalous Hall effect and intrinsic magneto-optical responses in mWSMs at zero external field [7–9]. Representative mWSMs including Co_2MnGa, $Co_3Sn_2S_2$ and Co_2TiGe demonstrate strong terahertz magneto-optical effects under zero field, with their magneto-optical strength jointly governed by Weyl node separation and Fermi level [10–13]. More critically, their off-diagonal dielectric tensor presents distinct effective refractive indices for left- and right-handed circularly polarized light, equipping the material with spin resolution free of external magnetic fields [14–16]. Nevertheless, the intrinsic absorption capacity of bare mWSMs remains insufficient for direct device implementation, necessitating appropriate photonic structures to effectively excite and tailor the spin-dependent absorption of the system [17, 18].

Periodic photonic crystal confine electromagnetic fields and enhance absorption via localized modes within their band gaps. As interface-localized electromagnetic modes, optical Tamm states (OTS) concentrate electromagnetic energy intensely at the interface between the functional layer and photonic crystal, representing an effective mechanism for near-perfect absorption (PA) [19–21]. Previous work has integrated mWSM with one-dimensional periodic photonic crystals to excite OTS at their interface, and the presence of these states leads to a difference between absorptivity and emissivity as high as 0.94 at a wavelength of 10 *μm*, thereby enabling nearly perfect nonreciprocal thermal radiation [22]. However, periodic photonic crystal possess simple band structures and typically support only one resonance channel, failing to meet the demand for multi-band spin-dependent absorption. By contrast, Fibonacci quasi-periodic photonic crystal features both long-range order and broken translational symmetry. Their self-similar fractal energy bands spontaneously generate multiple-order localized states across a broad spectral range, enabling multi-channel optical responses without defect layers [23, 24]. This strategy has been adopted to realize graphene-based multi-channel terahertz perfect absorption [25–27]. While the intrinsic magneto-optical effect of mWSMs shows broad application potential, the combination of mWSMs with Fibonacci quasi-periodic photonic crystal remains unexplored for spin-dependent absorption. Especially, the multi-band absorption performance, independent tuning mechanism of each band, and the synergistic physics between OTS modes and magneto-optical effects in this zero-field system all require systematic investigation.

In this work, we construct a heterostructure composed of an mWSM thin film and a Fibonacci quasi-periodic photonic crystal to investigate its absorption properties in the mid- to far-infrared regime via the 4×4 transfer matrix method (TMM). Driven by the synergy between multi-order OTS modes and the intrinsic magneto-optical effect of mWSM, the structure exhibits triple-band spin-dependent near-PA at zero magnetic field. We further analyze the modulation rules of Weyl node separation, Fermi level, spacer parameters and dielectric thickness on the resonance frequency, amplitude and spin splitting of the three absorption bands, and clarify the physical mechanism based on the OTS phase matching condition. This work breaks the channel count limitation of periodic configurations and provides a theoretical basis for multi-band spin-dependent absorption devices.

Models and methods

We propose a heterostructure composed of an mWSM layer, a dielectric spacer layer, and a one-dimensional Fibonacci quasi-periodic photonic crystal. The schematic diagram of the proposed structure is depicted in Fig. 1. A perfect electric conductor (PEC) layer is introduced to suppress transmission completely, which ensures that the absorption A can be simply calculated as $A = 1\text{-}R$, where R denotes the reflectance. The Fibonacci quasi-periodic photonic crystal is constructed from two dielectric layers A and B arranged according to the following recursive generation rule [28]:

$$G_1(n) = S_1 = B$$
$$G_2(n) = S_2 = B^{n-1}A$$
$$G_3(n) = S_3 = \left(B^{n-1}A\right)^n B$$
$$G_j(n) = S_j = S_{j-1}^n S_{j-2} (j \geqslant 4)$$

1

where *j* is the generation order of the Fibonacci sequence, and *n* is the repetition coefficient of the sequence (a positive integer). The relative permittivities of layers A and B are ε_A = 1.9044 (MgF_2) [29] and ε_B = 5.0625 (ZnS) [30], respectively. Their thicknesses are denoted as d_A and d_B. The dielectric spacer layer has a refractive index n_d = 1.45 (SiO_2) and a thickness of *d*. The C layer represents an mWSM layer with a thickness of d_c=400 nm. Transverse Magnetic (TM) polarized light waves are vertically incident from the air onto the mWSM layer.

The dielectric constant of the mWSM is achievable represented by a 3×3 tensor, owing to its inherent time-reversal symmetry-breaking property [31–33]:

$$\bar{\bar{\varepsilon}}_C = \begin{bmatrix} \varepsilon_d & i\varepsilon_a & 0 \\ -i\varepsilon_a & \varepsilon_d & 0 \\ 0 & 0 & \varepsilon_d \end{bmatrix}$$

2

where the expression for the off-diagonal element ε_a reads [31–33]:

$$\varepsilon_a = \frac{be^2}{2\pi^2\hbar\omega}$$

3

the diagonal element ε_d describes the conventional dielectric response of mWSM, including contributions from background lattice polarization and intraband/interband electronic transitions. Using the Kubo-Greenwood formula within the random phase approximation (RPA) two-band model (with spin degeneracy), we derive the conductivity σ and obtain the expression forε_d:

$$\varepsilon_d = \varepsilon_b + \frac{i\sigma}{\varepsilon_0\omega}$$

4

where ε_b is the background relative permittivity of mWSM from lattice ionic polarization, and σ is the complex conductivity of mWSM with the full form [31–33]:

$$\sigma = \frac{e^2 g k_F \Omega G\left(\frac{\Omega}{2}\right)}{24\pi\hbar} + \frac{ie^2 g k_F}{24\pi^2\hbar}\left[\frac{4}{\Omega} + \frac{4\pi^2}{3\Omega}\left(\frac{k_B T}{E_F}\right)^2\right] + \frac{ie^2 g k_F}{3\pi^2\hbar}\Omega\int_0^{\xi_c}\frac{G(\xi) - G\left(\frac{\Omega}{2}\right)}{\Omega^2 - 4\xi^2}\xi d\xi$$

5

where *g* represents the number of Weyl node pairs, $k_F = E_F/(\hbar\nu_F)$ is the Fermi momentum, $\Omega = \hbar(\omega + i\tau^{-1})/E_F$ represents the normalized complex frequency, *G(E) = n(-E)-n(E)* is the Fermi distribution difference function, *n(E)* represents the Fermi-Dirac distribution, k_B is the Boltzmann constant, *T* is the thermodynamic temperature, E_F represents the Fermi level, v_F is the Fermi velocity, τ represents the electron relaxation time, $\xi_C = E_C/E_F$ represents the normalized cutoff energy, and ξ is the normalized energy integration variable. Unless otherwise stated, all parameters in this work are taken from reference [34] : ε_b = 6.2, ξ_C = 3, τ = 1000 ps, *g* = 2, v_F=8.3×10^4 m·s^{-1}, *T* = 300 K, and E_F=0.3 eV.

To study the light absorption of this structure, we must first obtain its Fresnel reflection coefficient. The off-diagonal element of mWSM necessitates replacing the 2×2 TMM with the full-vector 4×4 TMM anisotropic formalism to accurately compute the reflection coefficients of right-handed circular polarization (RCP) and left-handed circular polarization (LCP) light and capture their anisotropic response [34], with R_+ and R_- defined as the reflection coefficients for RCP and LCP light, respectively. Light transmission through the proposed structure is effectively suppressed by an integrated PEC substrate. Therefore, the absorption response for both LCP and RCP illumination can be acquired from the proposed heterostructure, which is expressed as A_-=1-R_- and A_+=1-R_+, respectively.

The 4×4 anisotropic TMM is employed to rigorously derive the reflection coefficients of RCP/LCP light, and to characterize the spin-dependent PA of the designed structure. The heterostructure comprises sequentially stacked layers (incident direction, left to right): mWSM layer C, spacer layer D, a one-dimensional Fibonacci quasi-periodic photonic crystal, and a bottom PEC substrate. The incident medium is air, and the cumulative transfer matrix M_{total} equals the product of the transfer matrices of all constituent layers [17, 35]:

$$M_{\text{total}} = (D^{(0)})^{-1} M_C M_D (M_B{}^{N-1} M_A)^N M_B D^{(0)}$$

6

where the matrices $D^{(l)}$ and $M_{(l)}$ corresponding to the *l*-th layer are expressed as [17, 35]:

$$D^{(l)} = \begin{bmatrix} 1 & 1 & 0 & 0 \\ N_+{}^{(l)} & -N_+{}^{(l)} & 0 & 0 \\ 0 & 0 & 1 & 1 \\ 0 & 0 & N_-{}^{(l)} & -N_-{}^{(l)} \end{bmatrix}$$

7

$$M_{(l)} = \begin{bmatrix} \cos(\varphi_+^{(l)}) & (i/N_+^{(l)})\sin(\varphi_+^{(l)}) & 0 & 0 \\ iN_+^{(l)}\sin(\varphi_+^{(l)}) & \cos(\varphi_+^{(l)}) & 0 & 0 \\ 0 & 0 & \cos(\varphi_-^{(l)}) & (i/N_-^{(l)})\sin(\varphi_-^{(l)}) \\ 0 & 0 & iN_-^{(n)}\sin(\varphi_-^{(l)}) & \cos(\varphi_-^{(l)}) \end{bmatrix}$$

8

where $\varphi_\pm^{(l)} = \frac{\omega}{c} N_\pm^{(l)} d^{(l)}$ gives the phase shifts of RCP and LCP waves in the *l*-th layer, $N_\pm^{(l)} = \sqrt{\varepsilon_d^{(l)} \pm i\varepsilon_a^{(l)}}$ represents their refractive indices, $d^{(l)}$ represents the *l*-th layer thickness, and *c* represents the speed of light in vacuum [36]. The relative permittivity tensors for the isotropic layers A and B can be expressed as [17, 35]:

$$\underset{A}{\overline{\overline{\varepsilon}}} = \begin{bmatrix} \varepsilon_A & 0 & 0 \\ 0 & \varepsilon_A & 0 \\ 0 & 0 & \varepsilon_A \end{bmatrix}, \underset{B}{\overline{\overline{\varepsilon}}} = \begin{bmatrix} \varepsilon_B & 0 & 0 \\ 0 & \varepsilon_B & 0 \\ 0 & 0 & \varepsilon_B \end{bmatrix}$$

9

in addition, the reflection coefficients of RCP and LCP waves can be expressed as [17, 35]:

$$r_+ = \frac{M_{21}}{M_{11}}, r_- = \frac{M_{43}}{M_{33}}$$

10

Thus, the reflectances of RCP and LCP waves are denoted as $R_+ = |r_+|^2$ and $R_- = |r_-|^2$, respectively. The absorption of RCP and LCP waves are denoted as $A_+ = 1 - R_+$and$A_- = 1 - R_-$ respectively. In the following discussion, we mainly investigate the realization and tunability of triple-band spin-dependent near-PA.

Results and discussion

To clarify the excitation frequency range of OTS, we first construct a reference structure excluding the mWSM layer and calculate its reflectance spectrum, as depicted in Fig. 2(a). In the band from 39.0 to 43.0 THz, the quasi-periodic structure forms three high-reflectance photonic band gaps with reflectance close to 100%, centered at approximately 39.5 THz, 40.9 THz, and 42.3 THz. This provides a structural basis for the simultaneous excitation of multi-band interfacial localized states. After integrating the mWSM layer onto the incident side of the reference structure, the absorption and reflection phase spectra of the composite structure are shown in Fig. 2(b). In this work, parameters *j* and *n* are set to 3

and 6, respectively. The optimized unit cell parameters are as follows: d = 2.63 *μm*, d_A = 1.05 *μm*, and d_B = 9 *μm*. Extremely narrow resonant absorption peaks with near-unity absorption emerge within all three corresponding photonic band gaps, achieving triple-band near-perfect light absorption. The central frequencies of the three absorption peaks are 39.26 THz, 40.69 THz, and 42.13 THz, respectively, which match closely with the band gap centers of the reference structure. This indicates that the absorption resonant modes are strictly confined within the photonic band gaps, in accordance with the frequency characteristics of interfacial localized electromagnetic modes. As shown in the reflection phase curves of Fig. 2(b), abrupt phase jumps occur at all three resonant frequencies, which is a typical signature of OTS excitation and satisfies the total phase matching condition of integer multiples of 2π. This directly confirms that all three narrow-band absorption peaks originate from OTS excited at the spacer layer between the mWSM layer and the quasi-periodic photonic crystal. Figure 2(c) presents absorption spectra for incidence of LCP and RCP light. Pronounced spin splitting can be clearly observed across the three absorption bands, where the resonant frequency and peak absorptance of the absorption peaks show significant discrepancies for LCP and RCP light.

We then examine the modulation of LCP and RCP absorption by the Weyl node separation b and Fermi level E_F. As seen in Fig. 3(a) and 3(c), RCP absorption peaks monotonically with increasing *b*, while LCP peaks blueshift, enlarging their frequency separation. This is because the off-diagonal element ε_a grows linearly with *b*, increasing the effective refractive index N_+ for RCP and lowering its resonant frequency, while decreasing N_- for LCP and raising its resonant frequency, thus amplifying spin splitting. The peak absorptance of the three main resonances stays above 0.93 across the full *b* tuning range, retaining near-PA even at $b = 1.5\times10^9$ m^{-1}. The strong field localization of OTS ensures sufficient light-matter interaction, so that *b* induced loss variation does not significantly weaken the main absorption peaks. As shown in Figs. 3(b) and 3(d), raising E_F from 0.28 eV to 0.32 eV uniformly blueshifts all three absorption peaks for both polarizations. A higher Fermi level increases the Fermi momentum k_F, reducing the real part of the mWSM effective permittivity and hence the effective refractive index. Per the OTS resonant phase condition, a lower refractive index yields a higher resonant frequency, causing an overall blueshift. Peak absorptance decreases slightly with E_F but remains above 0.92, still in the near-PA regime, as the strongly localized main resonances are insensitive to small loss fluctuations. Notably, the LCP and RCP splitting magnitude for each resonance order is nearly invariant under E_F tuning. Since spin splitting is dominated by ε_a, which is primarily governed by *b* and insensitive to E_F, the Fermi level enables continuous dynamic tuning of the operating band without modifying the spin selection characteristics.

We next investigate tunable triple-band near-PA via spacer layer thickness d and refractive index n_d. Figures 4(a) and 4(c) present the absorption spectra of right- and left-handed circularly polarized light at spacer layer thicknesses d of 2.53 *μm*, 2.63 *μm*, and 2.73 *μm*, respectively. It can be observed that the absorption peak positions undergo a synchronous redshift with increasing thickness, whereas the evolution trends of peak absorption intensity for the two circular polarizations show marked divergence. For RCP light, the peak intensities of the three absorption peaks decrease monotonically as the spacer layer thickness rises from 2.53 *μm* to 2.73 *μm*. At d = 2.53 *μm*, the RCP absorptance A_+ in all three

frequency bands approaches 1.0. When d increases to 2.63 *μm*, the peak absorptance drops to approximately 0.92. At *d* = 2.73 *μm*, the peaks further decline to the range of 0.6–0.7. For LCP light, the absorption peak follows a non-monotonic trend of first increasing and then decreasing with growing thickness. At *d* = 2.53 *μm*, the peak value of LCP absorptance A_- is around 0.80. When d reaches 2.63 *μm*, the peak rises to about 0.95, approaching near-PA. As d further increases to 2.73 *μm*, the peak decreases slightly but remains near 0.9. The physical origin of this differentiated evolution lies in the difference in effective refractive index corresponding to the two circular polarizations. RCP light is associated with a larger effective refractive index N_+ which means that a smaller physical thickness of the spacer layer is required to satisfy the OTS phase matching condition. Accordingly, the phase matching condition can be satisfied at a smaller spacer layer thickness. In contrast, LCP light corresponds to a smaller effective refractive index N_- and thus a longer equivalent cavity length, so its optimal field localization occurs at a larger spacer layer thickness.

Figures 4(b) and 4(d) show the absorption spectra of RCP and LCP light at spacer layer refractive indices n_d of 1.35, 1.45, and 1.55, respectively. Like the regulation behavior of thickness tuning, an increase in refractive index also induces a synchronous redshift of the absorption peak positions, while the evolution of absorption intensity for the two circular polarizations exhibits marked asynchronism. For right-handed RCP light, the peak absorptance decreases monotonically with rising refractive index. At n_d =1.35, the RCP absorptance A_+ in all three frequency bands approaches 1.0, achieving near-PA. When n_d increases to 1.45, the peak value drops to approximately 0.9. At n_d =1.55, the peak declines substantially to around 0.5.For LCP light, the peak absorptance follows a non-monotonic trend of first increasing and then decreasing with growing refractive index. At n_d =1.35, the peak value of A_- is only about 0.6, corresponding to low absorption efficiency. When n_d reaches 1.45, the peak rises to above 0.95, attaining a near-PA state. As n_d further increases to 1.55, the peak decreases slightly but remains at approximately 0.9. This phenomenon is directly governed by the difference in impedance matching conditions between the two circular polarizations. Located between the air incident medium and the composite structure, the spacer layer functions as an impedance transition layer. When the refractive index of the spacer layer is close to the geometric mean of the equivalent refractive indices of air and the structure, interfacial reflection is minimized and absorption efficiency is maximized. Since the structure corresponding to RCP light has a higher equivalent refractive index, a lower spacer layer refractive index is sufficient to realize impedance matching and achieve optimal absorption. In contrast, the structure corresponding to LCP light has a lower equivalent refractive index, so a higher spacer layer refractive index is required to reach optimal impedance matching.

Finally, we examine the impact of layer thicknesses of media A and B in the quasi-periodic photonic crystal on triple-band spin-dependent near-PA. In Figs. 5(a) and 5(c), increasing d_A from 0.95 to 1.15 *μm* induces a synchronous redshift of all three absorption peak centers. The photonic band gaps of the Fibonacci quasi-periodic structure originate from multiple interfacial reflections and interferences, and the localized resonant modes satisfy the equivalent cavity condition: total optical thickness scales positively with resonant wavelength. A larger d_A raises the unit optical thickness ($n_A \cdot d_A$), lengthening the

resonant wavelength and lowering the resonant frequency. All three peaks, corresponding to different-order quasi-periodic localized modes, follow the same interference law, yielding a uniform redshift. As shown in Figs. 5(b) and 5(d), raising d_B from 8.95 to 9.05 μm also redshifts the three main peaks, with a far greater magnitude than d_A at comparable relative variation. As the core unit for Bragg reflection and band gap formation, the high-index ZnS layer B occupies a larger fraction of the structure. Minor d_B changes cause substantial variations in total optical thickness, delivering much higher frequency tuning sensitivity than the low-index layer A. Furthermore, d_B variation triggers pronounced mode splitting in the quasi-periodic band structure. Deviating d_B from the optimal value generates multiple secondary peaks between the original three main peaks, increasing absorption channels. This is attributed to Fibonacci quasi-periodic structures feature self-similar bands and broken translational symmetry, where small perturbations split localized modes and generate extra localized states. A comparison shows that both d_A and d_B enable continuous peak tuning, but differ fundamentally in sensitivity, mode evolution, and mechanism. The high-index layer B offers higher tuning efficiency, where small thickness changes yield large frequency shifts, while the low-index layer A produces gentler frequency modulation. The d_A mainly adjusts the absorption intensity of main modes and preserves the stable triple-band structure, whereas d_B readily induces band splitting and forms multi-peak absorption.

Conclusions

In summary, we have demonstrated triple-band spin-dependent near-perfect absorption without external magnetic fields in an mWSM–Fibonacci quasi-periodic photonic crystal heterostructure. The absorption originates from OTS, which satisfy the phase-matching condition at three resonant frequencies within distinct photonic band gaps. Each band exhibits pronounced spin splitting, with distinct shifts in resonant frequency and peak absorptance for LCP and RCP light. Parameter studies reveal that the Weyl node separation and Fermi level govern the magneto-optical strength and spin-splitting degree, while the spacer and dielectric layer thicknesses enable continuous frequency tuning. Among all constituent layers, the high-index ZnS layer offers the highest tuning sensitivity, owing to its dominant role in Bragg reflection. With these independent control knobs, the three absorption bands can be flexibly tailored in both frequency and intensity. Accordingly, this design overcomes the single-channel limitation of periodic photonic structures and opens an avenue toward integrated multi-channel spin-dependent photonic devices.

Declarations

Funding This work was partially supported by the National Natural Science Foundation of China (Grant No. 62605136), the Natural Science Foundation of Hunan Province (Grant No. 2026JJ80072), the Education Department of Hunan Province (Grant Nos. 23B0571 and 25A0425), and the Supported by Scientific research and innovation Foundation of Hunan University of Technology (Grant No. CX2509).

Data Availability All data in support of the findings of this paper are available within the article.

References

1. Inoue M, Fujikawa R, Baryshev A, et al (2006) Magnetophotonic crystals. J Phys D Appl Phys 39:R151–R161
2. Wei Z, Yang Y, Wu D, et al (2025) Recent development of magneto-optical thin films and integrated photonic devices. J Mater Chem C 13:12628–12649
3. Bhandia R, Cheng B, Brown-Heft TL, et al (2020) Thz-range Faraday rotation in the Weyl semimetal candidate Co_2TiGe. J Appl Phys 128:244303
4. Hu Y, Xie S, Bai C, et al (2022) Quasi-bound states in the continuum enabled strong terahertz chiroptical response in bilayer metallic metasurfaces. Crystals 12:1052
5. Dong D, Liu Y, Fu Y (2020) Enhancing the Faraday rotation of monolayer black phosphorus by the optical Tamm state at the photonic crystal interface. Appl Opt 59:9607
6. He J, He X, Dong T, et al (2022) Recent progress and applications of terahertz metamaterials. J Phys D Appl Phys 55:123002
7. Yan B, Felser C (2016) Topological materials: Weyl semimetals. Annu Rev Condens Matter Phys 8
8. Nagaosa N, Morimoto T, Tokura Y (2020) Transport, magnetic and optical properties of Weyl materials. Nat Rev Mater 5:621–636
9. Armitage NP, Mele EJ, Vishwanath A (2018) Weyl and Dirac semimetals in three-dimensional solids. Rev Mod Phys 90:015001
10. Jadidi MM, Mittendorff M, Aytac Y, et al (2018) Time-resolved terahertz magneto-optical study of the Weyl semimetal TaAs. APS March Meeting 2018
11. Trépanier O, Duchesne RN, Boudreault JJ, et al (2022) Magneto-optical Kerr effect in Weyl semimetals with broken inversion and time-reversal symmetries. Phys Rev B 106:125104
12. Parent J-M, Côté R, Garate I (2020) Magneto-optical Kerr effect and signature of the chiral anomaly in a Weyl semimetal in magnetic field. Phys Rev B 102:245126
13. Yan B, Felser C (2017) Topological materials: Weyl semimetals. Annu Rev Condens Matter Phys 8:337–354
14. Zhao B, Guo C, Garcia CAC, et al (2020) Axion-field-enabled nonreciprocal thermal radiation in Weyl semimetals. Nano Lett 20:1923–1927
15. Bednik G, Tikhonov K, Syzranov S (2020) Magnetotransport and internodal tunnelling in Weyl semimetals. Phys Rev Res 2:023124
16. Song Q, Zhou Z, Zhu G, et al (2022) Microdisk array-based Weyl semimetal nanofilm terahertz detector. Nanophotonics 11:3595–3602
17. Li T, Yin C, Wu F (2022) Giant enhancement of Faraday rotation in Weyl semimetal assisted by optical Tamm state. Phys Lett A 437:128103
18. He M, Li T, Yin C, et al (2023) Low-threshold bistable absorption in asymmetrical one-dimensional photonic crystals containing Weyl semimetal defects. Eur Phys J B 96:128

19. Kaliteevski M, Iorsh I, Brand S, et al (2007) Tamm plasmon-polaritons: Possible electromagnetic states at the interface of a metal and a dielectric Bragg mirror. Phys Rev B 76:165415
20. Tong RJ, Zhang RZ, Yuan PC, et al (2026) Tamm plasmon polaritons: Principle, excitation, and sensing applications. Laser Photonics Rev 20:e02507
21. Wu J, Liang Y, Guo J, et al (2020) Tunable and multichannel terahertz perfect absorber due to Tamm plasmons with topological insulators. Plasmonics 15:83–91
22. Wu J, Sun Y, Wu F (2023) Enhancing nonreciprocal thermal radiation in Weyl semimetals based on optical Tamm states by integrating with photonic crystals. J Mod Opt 70:187–196
23. Vyunishev AM, Pankin PS, Svyakhovskiy SE, et al (2017) Quasiperiodic one-dimensional photonic crystals with adjustable multiple photonic bandgaps. Opt Lett 42:3602–3605
24. Eyni Z, Milanchian K (2023) Optical properties of 1D quasiperiodic structures containing graphene-based hyperbolic metamaterials. Opt Quantum Electron 55:892
25. Wu J, Yang X, Wang Z, et al (2022) Tunable multichannel terahertz perfect graphene absorber with Fibonacci quasiperiodic photonic crystal. Adv Compos Hybrid Mater 5:2399–2405
26. Zhang P, Deng X-H, Liu H, et al (2022) Tunable enhanced THz absorption in Fibonacci photonic crystals with graphene. Eur Phys J D 76:163
27. Passler NC, Paarmann A (2017) Generalized 4×4 matrix formalism for light propagation in anisotropic stratified media: Study of surface phonon polaritons in polar dielectric heterostructures. J Opt Soc Am B 34:2128–2139
28. Gong Y, Liu X, Wang L, et al (2011) Multiple responses of TPP-assisted near-perfect absorption in metal/Fibonacci quasiperiodic photonic crystal. Opt Express 19:9759–9769
29. Palik ED (1998) Handbook of optical constants of solids. Academic Press
30. Zhu H, Luo H, Li Q, et al (2018) Tunable narrowband mid-infrared thermal emitter with a bilayer cavity enhanced Tamm plasmon. Opt Lett 43:5230–5233
31. Hofmann J, Das Sarma S (2016) Surface plasmon polaritons in topological Weyl semimetals. Phys Rev B 93:241402
32. Nagaosa N, Sinova J, Onoda S, et al (2010) Anomalous Hall effect. Rev Mod Phys 82:1539–1592
33. Kotov OV, Lozovik YE (2016) Dielectric response and novel electromagnetic modes in three-dimensional Dirac semimetal films. Phys Rev B 93:235417
34. Asadchy VS, Guo C, Zhao B, et al (2020) Sub-wavelength passive optical isolators using photonic structures based on Weyl semimetals. Adv Opt Mater 8:2000100
35. Wu J, Zeng R, Liang J, et al (2023) Spin-dependent and tunable perfect absorption in a Fabry-Perot cavity containing a multi-Weyl semimetal. Opt Express 31:30079–30091
36. Višňovský Š, Postava K, Yamaguchi T (2001) Magneto-optic polar Kerr and Faraday effects in magnetic superlattices. Czech J Phys 51:917–949

Figures

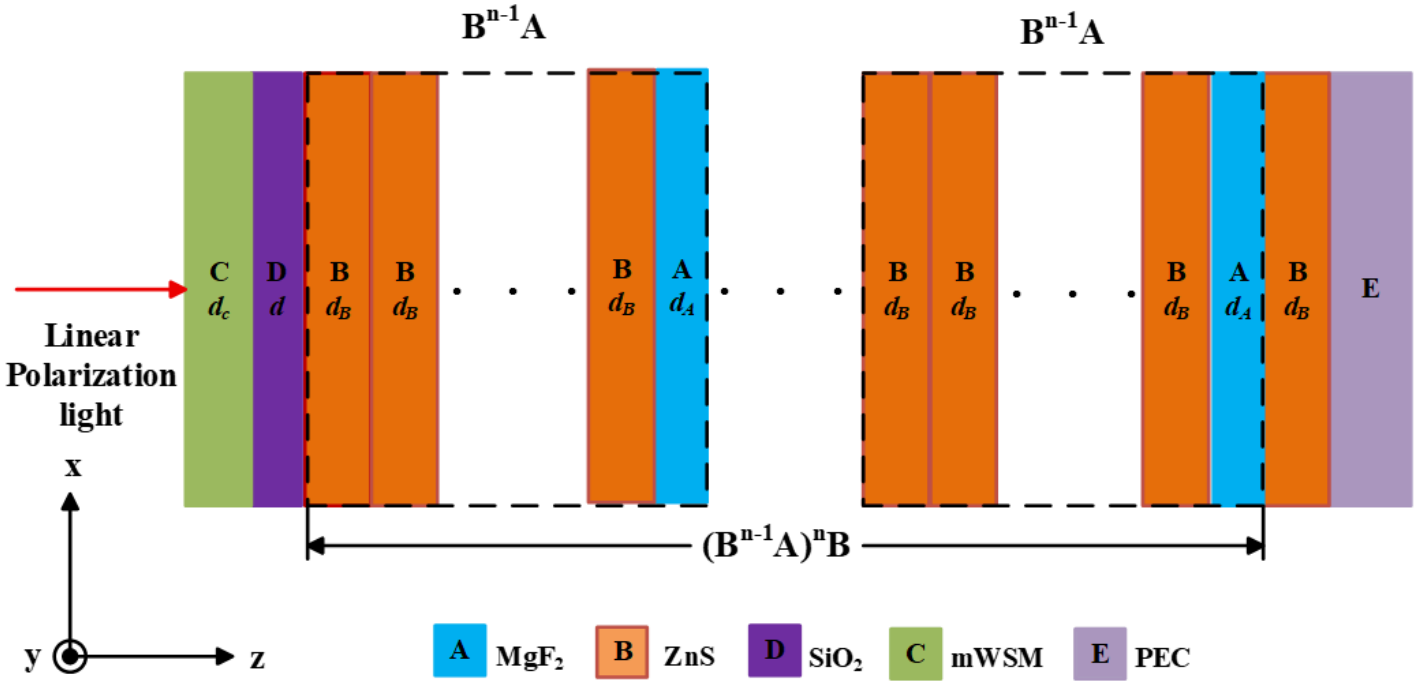


Figure 1

Schematic diagram of the proposed heterostructure for achieving multi-channel spin-dependent photonic absorption. The heterostructure consists of an mWSM layer, a spacer layer, and a one-dimensional Fibonacci quasi-periodic photonic crystal. Layer D denotes the spacer layer with thickness d, and layer C denotes the mWSM layer with thickness d_c. The two Weyl nodes of opposite chirality in the mWSM are aligned along the z-axis.

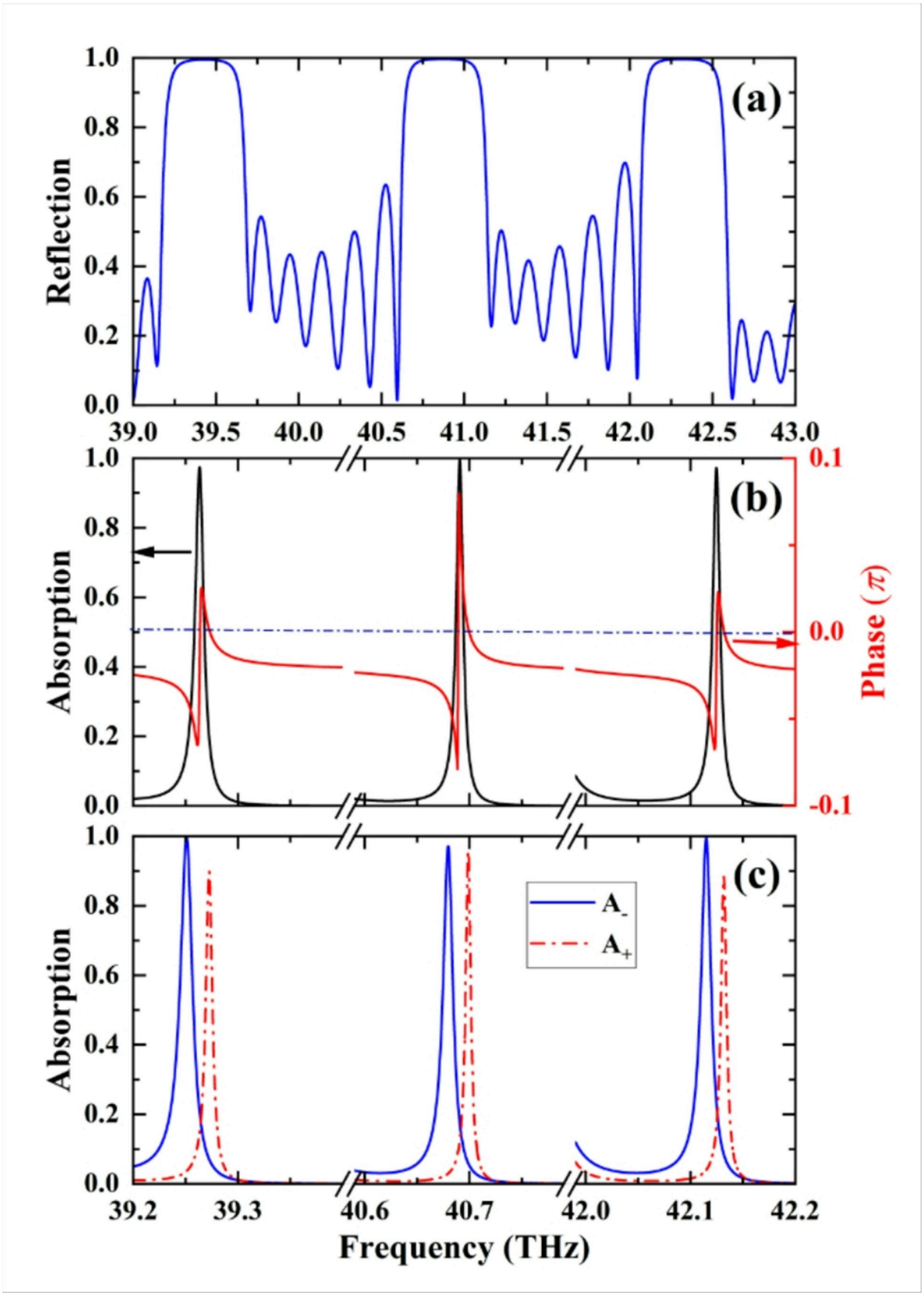


Figure 2

Spectral responses of the quasi-periodic photonic crystal. (a) reflectance of the reference structure (no mWSM layer). (b) absorption (blue, left axis) and reflection phase (red, right axis) of the hybrid structure. (c) absorption spectra for LCP (solid blue) and RCP (dashed red) light.

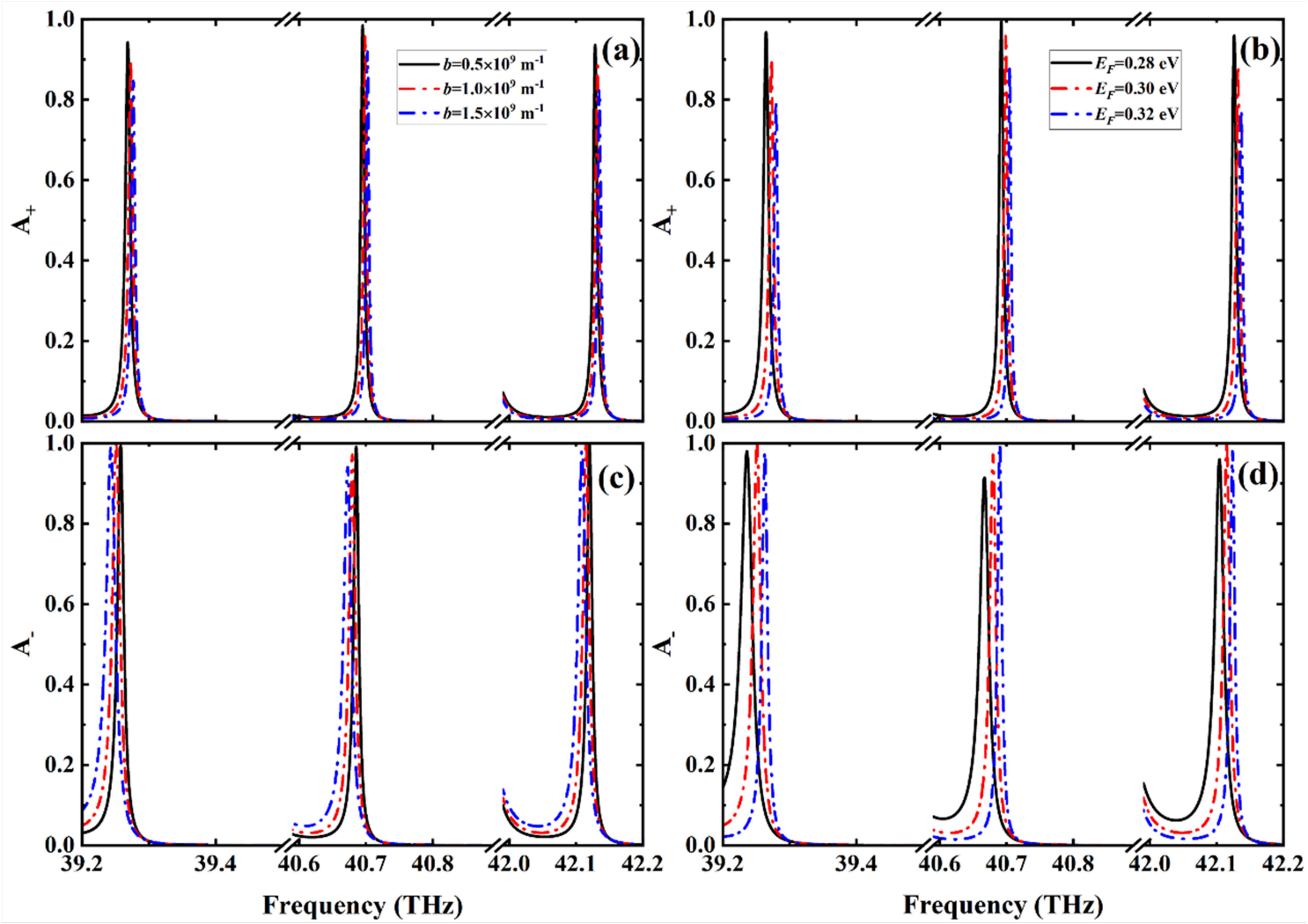


Figure 3

Triple-band spin-dependent near-PA is tunable via Weyl node separation and Fermi level. Panels (a) and (c) present the absorption spectra of LCP and RCP light for different values of the Weyl node separation *b*, while panels (b) and (d) show the corresponding spectra for different Fermi levels E_F.

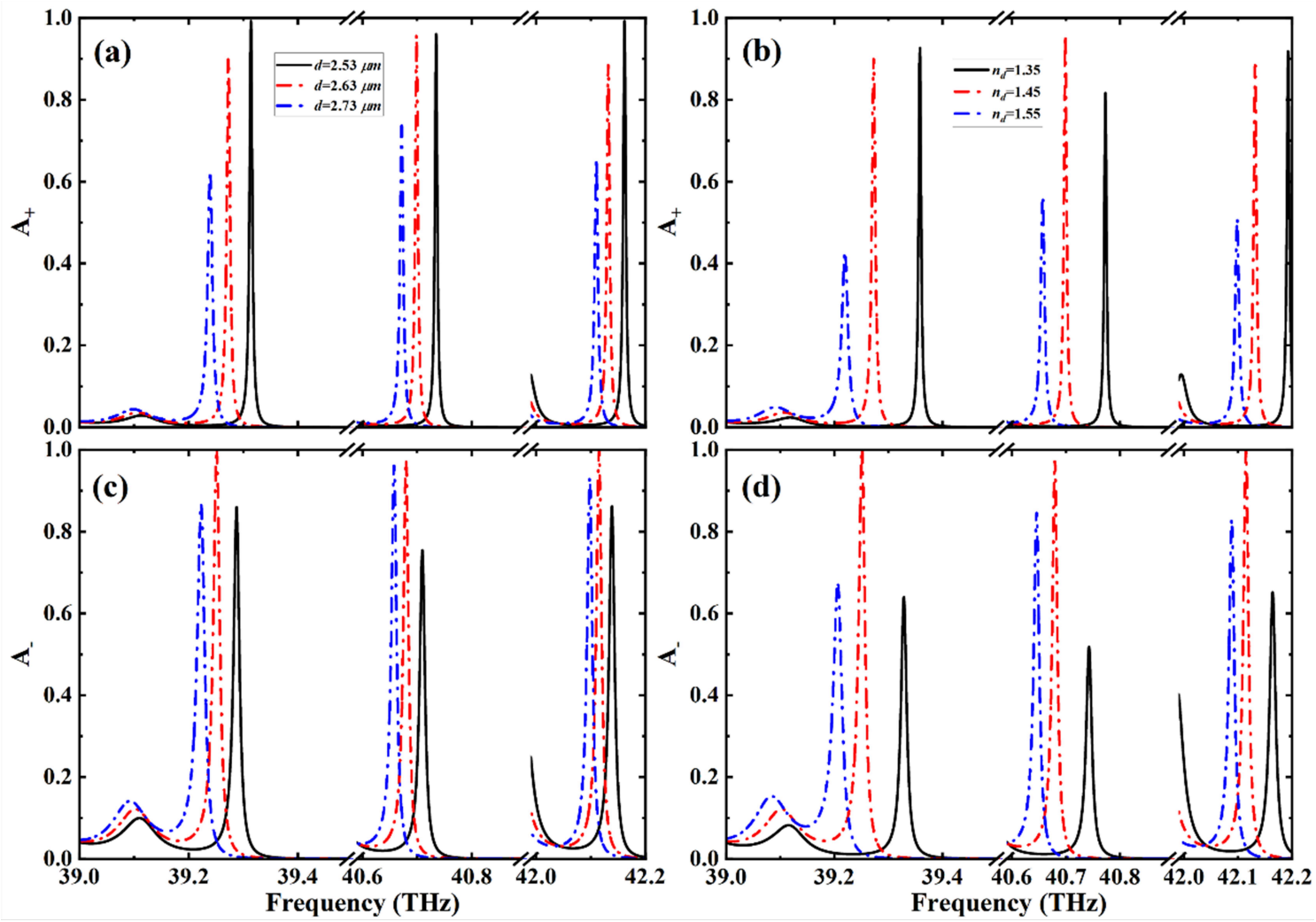


Figure 4

Spin-dependent absorption spectra under different spacer parameters. (a) and (c) absorptance versus incident frequency for LCP and RCP light at various spacer thicknesses. (b) and (d) absorptance versus incident frequency for LCP and RCP light at various spacer refractive indices.

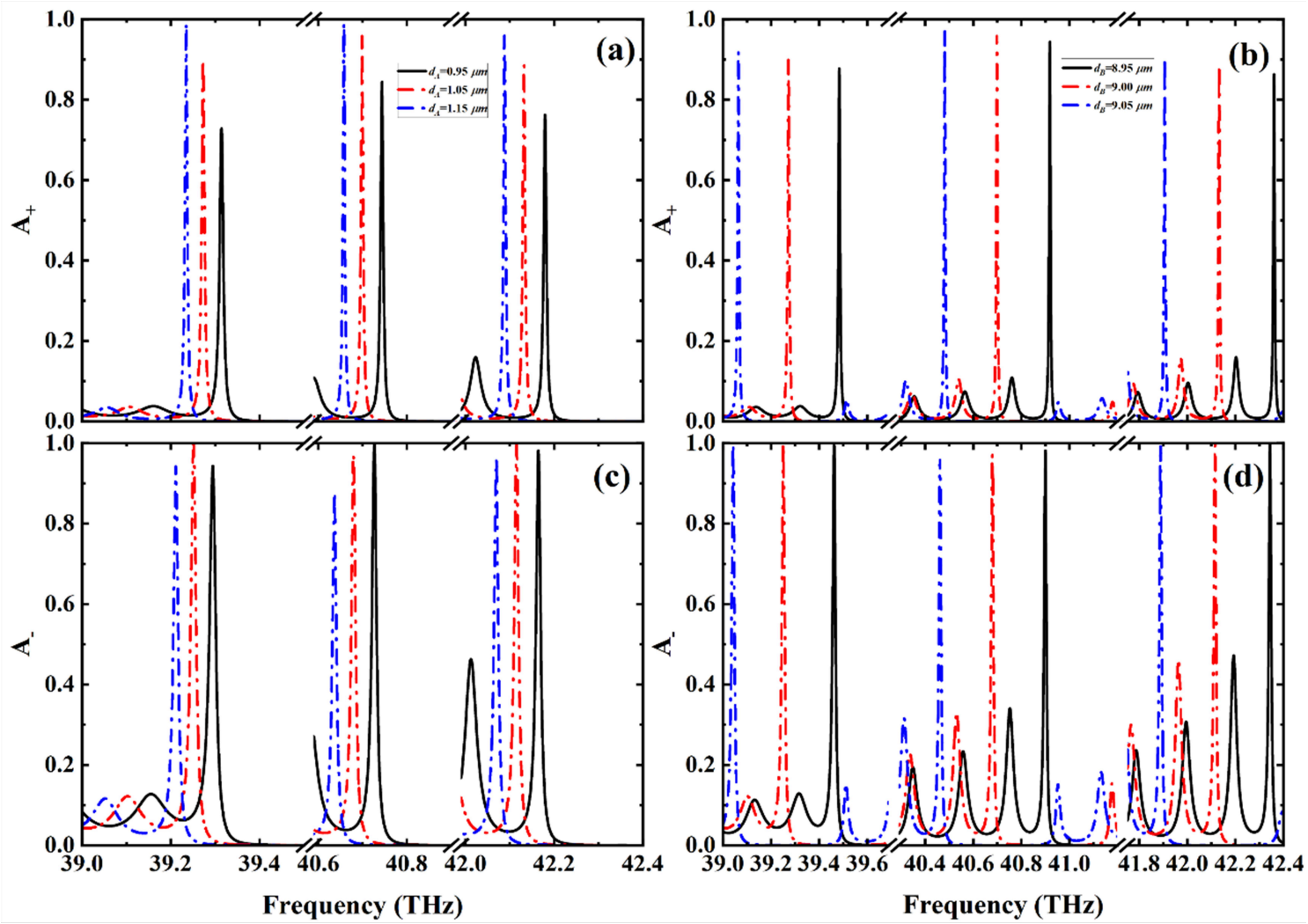


Figure 5

Modulation of spin-dependent absorption spectra by dielectric layer thicknesses. (a) and (c) absorptance versus frequency for LCP and RCP light at various d_A values. (b) and (d) absorptance versus frequency for LCP and RCP light at various d_B values.